Adaptive Surrogate-Based Optimization of Vortex Generators for a Tiltrotor Geometry *

R.L.T. Bevan†, D.J. Poole‡, C.B. Allen § and T.C.S. Rendall ¶
Department of Aerospace Engineering,

University of Bristol, Bristol, BS8 1TR, U.K.

Design of vortex generators (VGs) on a tiltrotor aircraft infinite wing is presented using an adaptive surrogate modelling approach. Particular design issues in tiltrotors produce wings that are thick and highly loaded, so separation and early onset buffet can be problematic and VGs are commonly used to alleviate these issues. In this work, the design of VGs for elimination of separation is considered using a viscous flowfield simulations. A large design space of rectangular vane-type vortex generators is sampled and simulated, and a radial basis function surrogate model is implemented to model the full design space. An efficient adaptive sampling approach for improved design space sampling has also been developed that balances the properties of space-filling, curvature capture and optimum locating. This approach has been tested on the design of a VG on a highly loaded infinite wing, with a representative tiltrotor airfoil section, using a five-dimensional design space. Design of the VGs using this approach shows that elimination of the separation is possible whilst simultaneously reducing the drag of the wing with optimized the VGs, compared to the clean wing.

---

* Previously presented as AIAA Paper 2015-2725 at 33rd AIAA Applied Aerodynamics Conference, Dallas, Texas, 2015
† Research Assistant, Email: r.bevan@bristol.ac.uk
‡ Research Assistant, Email: d.j.poole@bristol.ac.uk
§ Professor of Computational Aerodynamics. Email: c.b.allen@bristol.ac.uk
¶ Lecturer. Email: thomas.rendall@bristol.ac.uk

Nomenclature

AR = vortex generator aspect ratio

b = exploitative distance function

c = vortex generator leading edge stream-wise chord location

C = adaptive sampling criterion

C_b = exploitative adaptive sampling criterion

C_L, C_D, C_M = lift, drag and pitching moment coefficients

CR = crossover probability

d_1, d_2 = minimum and supremum distances between all sample points

f, g = generic functions

F = mutation rate

h = vortex generator height

H = distance function

J = objective function

k = objective comparison factor

l = vortex generator length

P = interpolation polynomial

q = interpolation model

r_1, r_2, r_3 = three random numbers ($0 \leq r_1, r_2, r_3 \leq 1$)

R = support radius

R_0 = distance scaling factor

s = vortex generator spacing ratio

S = airfoil separation percentage

$\hat{\mathbf{S}}$ = turbulence model variable

$\mathbf{S}_s$ = rate of strain tensor

u_∞ = freestream velocity

$\mathbf{u}$ = velocity field

$\mathbf{v}_n$ = donor vector

$\mathbf{w}, \boldsymbol{\gamma}$ = radial basis model coefficients

$\mathbf{x}$ = generic coordinate

y_1, y_2 = vortex generator spacings

α = airfoil incidence angle

Γ_p = circulation

δ = boundary layer height

ϵ = small, positive constant

θ = vortex generator angle relative to freestream

λ_2 = vortex extent criterion

ϕ = radial basis function

Ω = vorticity magnitude

$\boldsymbol{\Omega}_s$ = vorticity tensor

I. Introduction

Tiltrotor aircraft aim to combine the vertical lift capability of a helicopter with the speed and endurance of a conventional fixed-wing aircraft. In forward flight, the aircraft lift is provided by the wings. However, structural design considerations, such as whirl-mode stability and the necessity of sufficient internal wing volume for the drive mechanism, inhibit efficient aerodynamic performance. This results in very stiff, short span wings and a thick airfoil (for example, the Bell XV-15 utilised a NACA 64A223 [1]). Due to a short span and a typical cruise Mach number between 0.4 and 0.6, these low aspect ratio wings experience a high loading; a typical cruise lift coefficient for a tiltrotor being above 1.0. These design factors therefore make tiltrotor aircraft particularly susceptible to stall and early onset buffet, so boundary layer control is critical and upper surface flow control devices are an important consideration.

Flow control devices are regularly adopted in aerodynamic design, to control boundary layer behaviour, and are often retro-fitted where problems are identified. The most common methods are passive schemes, with vortex generators (VGs) the most conventional approach. These involve simple small flat plates normal to the surface, usually rectangular in shape, inclined to the freestream flow. The majority of VGs protrude into the external flow, i.e. above the boundary layer, but there have also been immersed, or sub-layer, VGs adopted [2].

The role of a VG is to induce vortical flow via the flow separation from its sharp upper edge. The vortex which subsequently propagates downstream entrains higher energy, higher momentum flow into the lower energy boundary layer. This re-energises the boundary layer, suppressing separation. For example, on the Bell XV-15 tiltrotor, VGs were utilised along the full wing span to eliminate premature stall and retain attached flow up to an angle of attack of 15 degrees[3]. Similar results were found when VGs were added to the V-22 Osprey tiltrotor wing [4] and fairing [5].

To understand and quantify the effects of VGs, simulation using computational fluids dynamics (CFD) methods is often employed [5–9]. However, the modelling of VGs by conventional CFD approaches poses difficult issues in capturing the vortex and its convection downstream. These simulations often require high-quality, fine numerical meshes on geometries where the size of the flow control device is orders of magnitude smaller than the global object. Both structured [10–13]

and unstructured meshes are common [14, 15]. Problems with meshing can be somewhat alleviated by using embedded VG models which mimic the effect of the VG, as opposed to modelling the VG itself [16–19].

Whether fully-gridded simulations or embedded simulations are performed, the type of physics that need to be captured tend to require simulations of the Reynolds-Averaged Navier-Stokes (RANS) equations. A suitable turbulence model must therefore also be selected. Two common turbulence models are Spalart-Allmaras (SA)[20] and k-ω SST[21], which have both been used to model flow around a VG [10, 11]. Yaras and Grosvenor [22] compared these models, and showed that, perhaps, SA demonstrated the best balance between prediction, robustness and computational efficiency. Alternatively, simulations via large eddy simulation (LES) or direct numerical simulation (DNS) can be performed [14, 23, 24], though at large computational cost.

A simulation method can also be integrated into the design optimization process. Linking the simulation to a numerical optimization routine allows the exploration of different designs of VGs to optimize some objective [25], which could be drag. The requirement for the simulation here, however, is to have sufficient fidelity physics to capture how changes to the VG design affect the final objective. An alternative approach to full numerical optimization is to link the simulation framework within surrogate-based analysis [26–28]. This approach uses a limited number of CFD simulations to sample the design space of the VGs. A surrogate then provides interpolation of the known sample points to obtain a continuous design space approximation away from the data sites. To increase the accuracy of the surrogate model, adaptive refinement after the initial construction can be useful in better capturing the optima in the design space [29]. A limited number of applications of surrogate-based design to VGs has been shown [30–32], demonstrating the feasibility of the approach to this design problem.

The work presented in this paper applies an adaptive surrogate modelling approach to the design of VGs on **an infinite wing with a representative tiltrotor airfoil section operating at** typical tiltrotor design requirements. First, a demonstration of the abilities of the chosen simulation approach to accurately capture the VG impact through comparison with experimental data is presented. Second, the quantification of flow around a tiltrotor airfoil with high fidelity CFD modelling

of vortex generators is detailed. These vortex generators are arranged in a counter-rotating array, where each pair consists of the rectangular vane type. A design space interrogation by statistical sampling and surrogate modelling is presented. Finally, exploitation of an optimum VG design via the surrogate model is presented and compared against the flow around a clean wing.

II. Simulation Framework

The capture of the physics of the flow around VGs requires high fidelity solvers and high density numerical meshes. A solution framework has been developed and involves obtaining viscous flows using OpenFOAM[59] with an autonomous mesh generation tool to produce high quality structured viscous meshes with a vortex generator.

A. Mesh Generation

A bespoke mesh generation tool was developed to generate high quality structured viscous meshes, both for the initial validation work and the representative airfoil sections (with and without a vortex generator).

The airfoil meshes generated had C-grid topology. A representative tiltrotor airfoil, which is a modified NACA 64(4)-421 section was used, with a 0.4% chord blunt trailing edge. A four-block structured multiblock mesh was generated [33], and three views are presented in figure 1; this is for a mesh with 769 points on the airfoil surface, 97 streamwise points on either side of the wake line, 65 points across the blunt trailing edge, and 129 points in the normal direction.

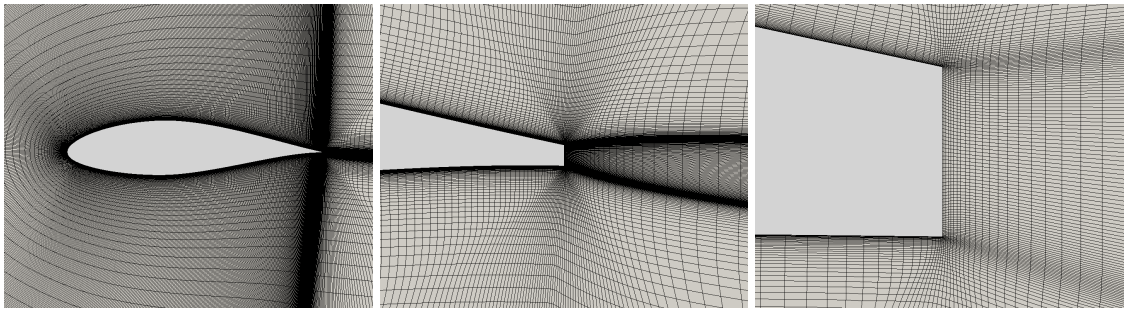

Fig. 1: Four-block structured mesh

[59] `http://www.OpenFOAM.org/`

To include the vortex generator, the two-dimensional mesh is extruded to the correct part-span position. A high quality mesh deformation scheme is then used to rotate the mesh to the required vortex generator incidence, and pull in mesh cells from upstream, downstream, above and either side of the generator to match the required local spacings. This is achieved via several local radial basis function deformations [34, 35]. The VG is then represented by a zero-thickness plane, which is designated using solid surface boundary conditions. Figure 2 shows the resulting wing surface mesh near the leading edge and the surface with starboard plane, together with a closer view of the VG.

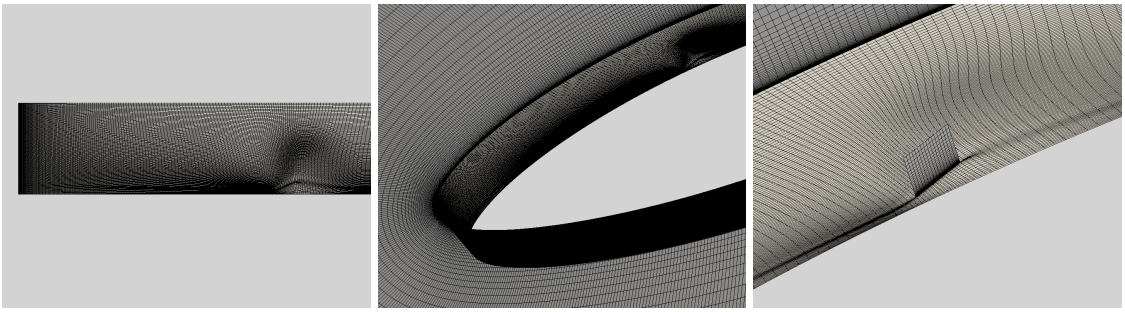

Fig. 2: Surface mesh including vortex generator

Validation of the simulation framework is presented below, and is performed on a VG on a flat plate. An example mesh is presented in figure 3. As is the case with the airfoil meshes, the vortex generator is represented by a zero-thickness plane. This plane, and the surrounding cells are also deformed using local radial basis function deformations to achieve the appropriate geometry and near-field resolution. Resolutions used were representative of those employed in the airfoil simulations, with 385 points on the flat plate streamwise direction and 129 in the spanwise direction. The normal direction has 129 points and 97 points extend streamwise to the farfield.

The final stage in the mesh generation process reduces the cell count away from sections of interest. This is undertaken through point removal and combining of hexahedral cells to form polyhedra. The mesh reduction process typically involves a 50-60% cell count reduction.

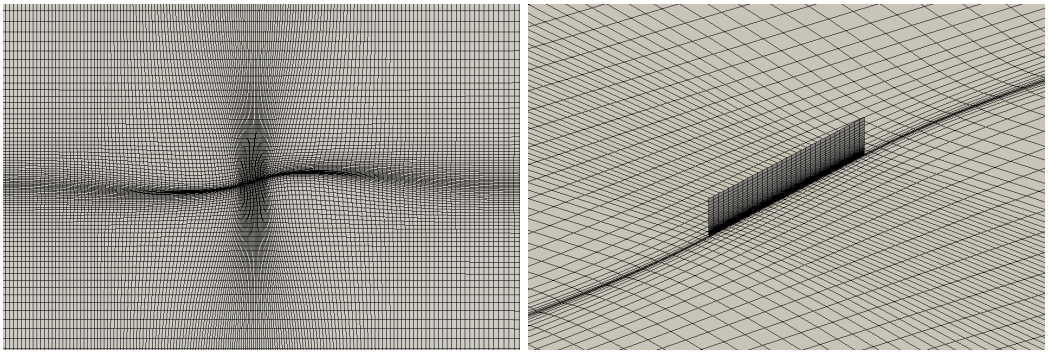

Fig. 3: Flat plate with inset VG (at 16 degrees)

B. Flow Solver

The solver package used in the current work is the open source CFD software OpenFOAM. The flow solver, with RANS turbulence modelling, is a unstructured solver based upon the SIMPLE algorithm (Semi-Implicit Method for Pressure-Linked Equations), which is an iterative procedure to solve the Navier-Stokes equations for steady-state problems. This iterative procedure, as originally implemented in OpenFOAM, relies on basic residual checking for steady-state convergence criteria. After modification, steady-state convergence is assessed using the standard deviation of the force coefficients. The turbulence model used was the standard Spalart-Allmaras (SA) model as defined by NASA Langley's Turbulence Modelling Resource[60], and has the minimum limiter of $0.3 \times \Omega$ for $\hat{S}$.

C. Framework Validation

A validation study was performed using experimental and complementary CFD data taken from the work of Yao *et al.* [36]. Although two rectangular vane-type VGs are studied experimentally, only one has accompanying numerical simulation results. It is this VG configuration which was considered within the current work to assert whether mesh resolution and quality is sufficient. This VG has a height, h, of 7mm (h/δ=0.2) and a length, l, of 49mm. Three VG angles of attack were tested (10, 16 and 23 degrees). The VG was located such that the boundary layer height was 35mm. At the inlet, fully turbulent conditions were assumed. Wall effects due to the wind tunnel were

[60] `http://turbmodels.larc.nasa.gov`

ignored and the domain extended 20m to the farfield from the 3m plate.

Figure 4 shows the circulation decay downstream of the VG and the spanwise vortex location. The circulation was determined during post-processing of the flow-field using a line integral along a positive x-vorticity contour. There is good agreement between the predicted circulation obtained via the RANS-SA OpenFOAM CFD and the experimental data. The applied method is sufficient to capture both the initial strength of the vortex and also the circulation downstream decay. The vortex core is tracked downstream using the same definition for the centre of the vortex as given in [36], namely the peak positive stream-wise vorticity component (within a given streamwise slice). As shown, the current CFD provides good agreement with the experimental results for the VGs angled at 16 and 23 degrees. The experimental results for the 10 degree VG are offset to both the current CFD and that undertaken by Yao *et al.* This is the smallest vortex, thus any errors are magnified somewhat.

From these results, it is evident that the chosen mesh resolutions and flow solver are sufficient to capture and track the strength and location of the vortex from the VG to beyond the distances measured in the experiment. Circulation decay was also accurately predicted by the current set-up. Of particular importance with regards to a design space investigation was the impact due to varying the VG angle, which was also accurately obtained.

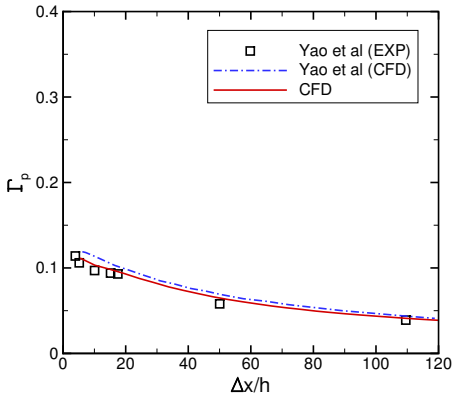

(a) Γ_p 10 degrees

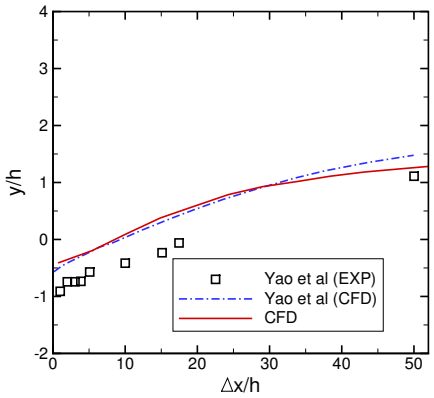

(b) y/h 10 degrees

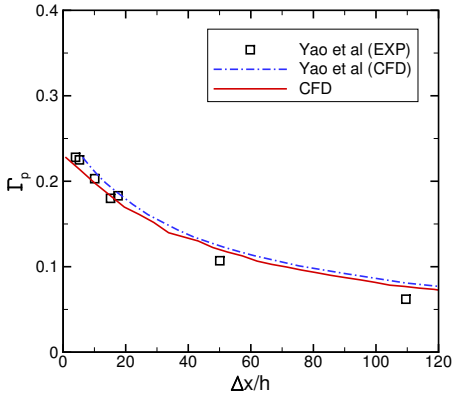

(c) Γ_p 16 degrees

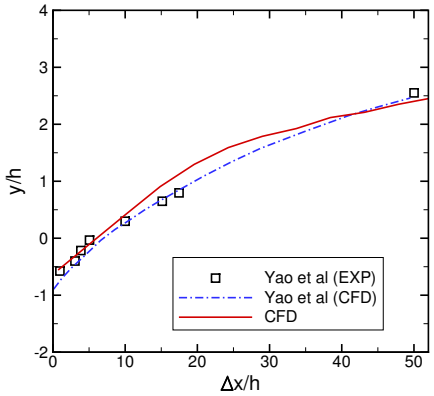

(d) y/h 16 degrees

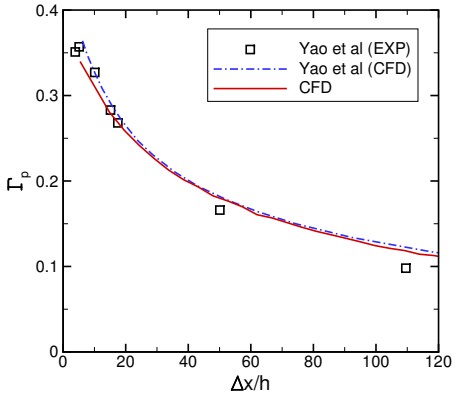

(e) Γ_p 23 degrees

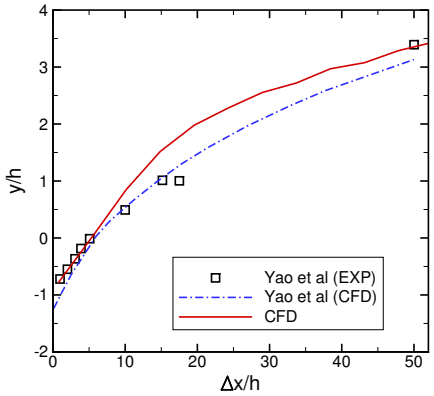

(f) y/h 23 degrees

Fig. 4: Circulation downstream and spanwise vortex path validation.

D. Design Flow Condition

Vortex generators on an aircraft are commonly added to modify unwanted flow phenomena at certain flight conditions on the flight envelope. Generally, this will not be in cruise conditions of the aircraft, but a point on the edge of the flight envelope. For a tiltrotor, which may have a cruise Mach number within the range of 0.4-0.6, the loading on the wing in cruise is low, hence the separation issues that create buffet and stall problems are not of concern. However, at the periphery of the flight envelope, these issues can arise.

Buffet is a particularly difficult flow phenomena to simulate due to its unsteady nature. However, it has been noted that buffet can be prominent on thick airfoils possibly due to the susceptibility of these airfoils to experience large separation regions [37]. A common empirical technique for predicting buffet onset is that due to Bore [38] and is drawn from the observation that buffet normally occurs when the wing is at its highest loading – and therefore likely experiencing separated flow. Bore postulates that buffet response is due to a deviation in the linearity of the lift coefficient curve, or the reverse of this which is that a change to the gradient of the lift-curve slope gradient is shifted to a higher lift coefficient. A similar method was also used by Kenway and Martins [39] to predict buffet onset of a transonic wing and subsequently perform shape optimization to mitigate against this onset. For the purpose of optimization, it is therefore appropriate to use the assumption that large separation regions are linked to buffet, hence steady-state simulations – which are capable of modelling separation – are used. Furthermore, for modelling vortices shed for VGs, steady-state simulations are appropriate [40]. As such, in this paper, buffet is not explicitly modelled (which would require unsteady simulations) but a steady-state cause of the buffet boundary is modelled and used for optimization purposes.

The design flow condition considered is representative of a highly-loaded case on the edge of the design envelope. As an example, the V-n diagram of the XV-15 [41] shows high loading factors. The example considered is similar to the XV-15 at maximum gross weight (15,000lb) at minimum forward velocity (150keas). At sea-level conditions this represents a Mach number of 0.24. The high

weight combined with low velocity and a small wing area results in a highly loaded wing, where the C_L is over 1.0, and when a loading factor is applied to this, for example during a manoeuvre, can give a much higher lift coefficient. These figures give an approximation of the types of loading that can be exhibited by the wing of a representative tiltrotor aircraft, hence the chosen design condition is similar in nature to this.

The VG optimization was undertaken at a Reynolds number of 7.5 million, and a Mach number of 0.24. The airfoil was trimmed to $C_L = 1.3$.

E. Airfoil Spanwise Boundary Conditions

To ensure proper choice of spanwise boundary conditions, representative airfoil simulations with the VG were undertaken using various spanwise boundary conditions. Three different geometry configurations were assessed. Since the simulations involve an infinite-wing, it is possible to utilise geometrical planes of symmetry to reduce the airfoil and VG section as shown in figure 5. While it is possible to utilise periodic boundary conditions as well as slip conditions for the double and single spans, it is only possible to use slip conditions on the half-span geometry. All five scenarios were examined.

In table 1, the converged force coefficients are presented for an example VG geometry. Convergence was determined when the standard deviation of each individual force coefficient was reduced below a tolerance of 1×10^{-4}, adjudged on the previous 30 iterations. The pitching moment coefficient was calculated about the quarter-chord point. From the table, it is clear that the choice of spanwise boundary condition is negligible when considering accuracy. Obviously, there is a significant computational cost with increasing the simulated domain. However, it is also necessary to examine flow conditions within the domain to determine boundary condition impact.

In figure 6, the λ_2 criterion is presented to quantify the vortex extent [42]. This criterion denotes the intermediate eigenvalue of the symmetric tensor $\mathbf{S}_s^2 + \mathbf{\Omega}_s^2$ where $\mathbf{\Omega}_s = \frac{1}{2}[\nabla\mathbf{u} - (\nabla\mathbf{u})^T]$ is the vorticity tensor and $\mathbf{S}_s = \frac{1}{2}[\nabla\mathbf{u} + (\nabla\mathbf{u})^T]$ the rate of strain tensor. Negative values of the λ_2 criterion denote the vortex. No discernible differences are evident as the geometry simulated is extended from the half span (slip) to a double span (periodic).

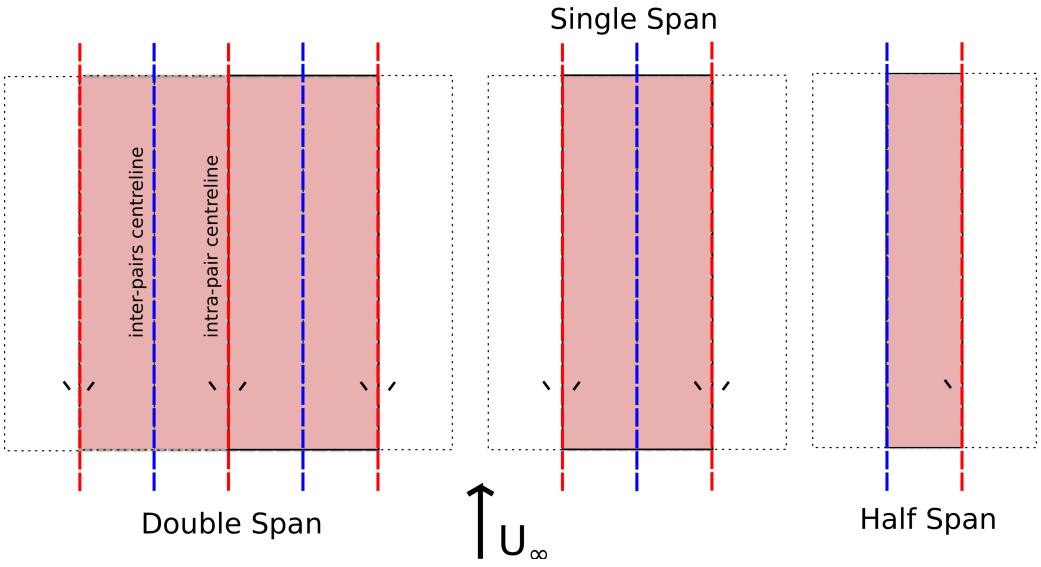

Fig. 5: Three geometry sections investigated

Table 1: Span geometry and boundary condition impact on force coefficients.

	Periodic BC		slip BC		
	Double Span	Single Span	Double Span	Single Span	Half-Span
C_L	1.2914	1.2915	1.2914	1.2915	1.2913
C_D	0.0262	0.0262	0.0262	0.0262	0.0262
C_M	-0.0858	-0.0858	-0.0858	-0.0858	-0.0858
Normalised CPU Cost	18.2	8.0	14.5	2.7	1.0

Since the spanwise boundary condition impact was negligible, the half-span with slip boundary condition was chosen due to its reduced computational cost.

III. Adaptive Surrogate Optimization Process

Implementation of the simulation framework to the VG design process was achieved by surrogate modelling. The CFD framework was used to simulate a number of VG designs to sample the VG design space, from which a surrogate model was constructed. This was then optimized to find an optimal VG design. The final design was rerun through the CFD framework to evaluate the predicted objective value from the surrogate with the real objective value from the CFD. If the error was large then new sample points were generated using an adaptive method and the process

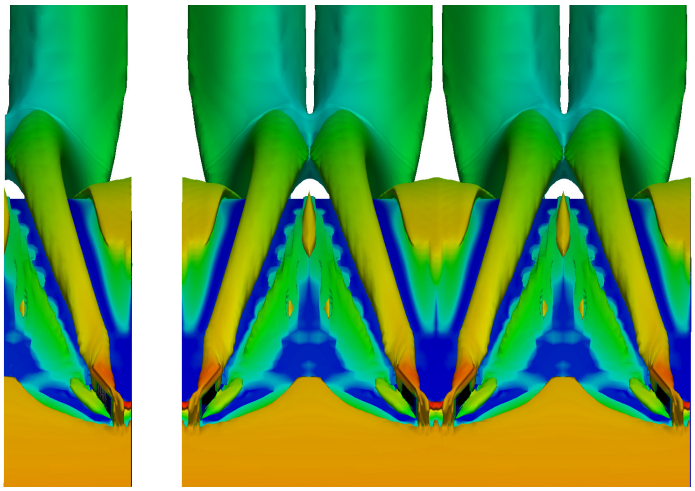

Fig. 6: Vortex extent, as denoted by $\lambda_2 = -0.1$ surface for the half-span (slip) and double span (periodic) setups.

was run again. The details of the surrogate model construction, including the suitable selection of initial sample points and adapted sample points, are presented in this section. A flowchart of the overall process is shown in figure 7.

A. Design Objective

While eliminating early onset buffet on tiltrotor wings is the overall objective, this can be undertaken by means of an intermediate objective which allows for only steady-state simulations. This intermediate objective is the elimination of the large separation which precedes buffet onset at the chosen design condition ($C_L = 1.3$). At the chosen design condition, a large separation region is observed beyond 88% airfoil chord, as shown in figure 8.

Vortex generators are added to reduce the separation region in figure 8, and therefore alleviate the early-onset buffet. Therefore the objective function (equation 1), against which to design the vortex generators, is chosen to be a compound objective, chosen to balance the design objective of reducing separation with the common objective of reducing drag. A compound objective function is chosen such that the reduction of the separation, which is the first goal of the optimization process, is considered explicitly by the optimizer, rather than implicitly if, say, drag were considered in isolation. Furthermore, if separation is eliminated, the optimizer can still reduce the objective

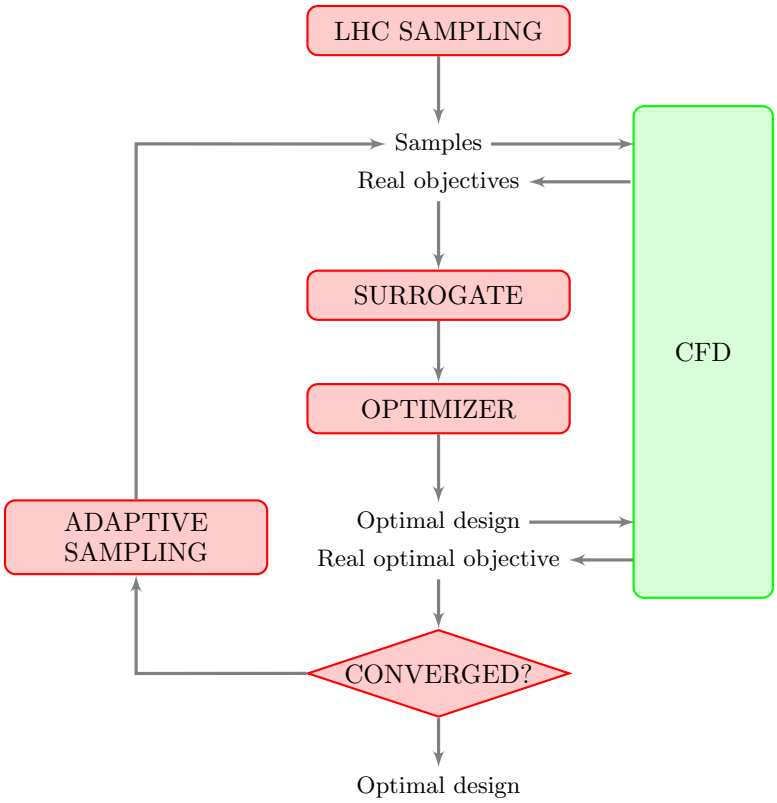

Fig. 7: Flowchart of adaptive surrogate design process

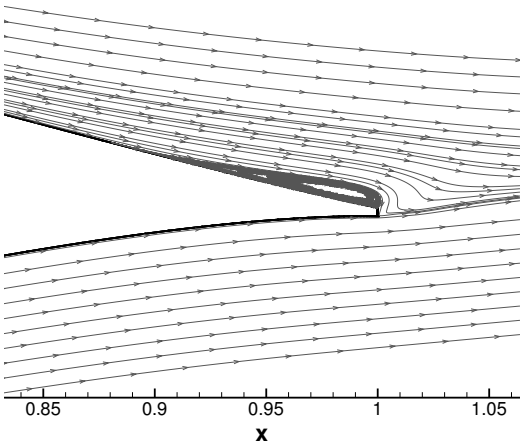

Fig. 8: Clean Geometry streamlines

function by considering the minimum drag VG to eliminate separation.

$$J = C_D + kS \tag{1}$$

In equation 1 J is the objective function to be minimized, S is the span-average separation chordwise location (as a percentage), and k is a constant used to balance the effect of the two. To ensure equal magnitude of both parameters, k is taken to be 0.0005 such that 1% separation equates to adding 5 drag counts to the problem. S is calculated as the ratio of the surface area of the upper surface that experiences a negative skin friction, to the total surface area of the airfoil's upper surface.

B. Design Parameters

In order to assess the efficiency and effectiveness of a chosen vortex generator design, the VG geometry must be classified by specific planform and location parameters. In this work, the VG geometry was classified by five such parameters, namely VG length (l), VG aspect ratio (AR), VG setting angle relative to freestream (θ), VG chordwise location (c) and the spacing ratio (s). The VG aspect ratio is defined as $AR = l/h$, and the spacing ratio is defined as the ratio between the intra-pair spacing (y_1) and the inter-pair spacing (y_2), where the intra-pair spacing is fixed ($y_1 = 0.5\%$). A schematic of the design geometry is shown in figure 9.

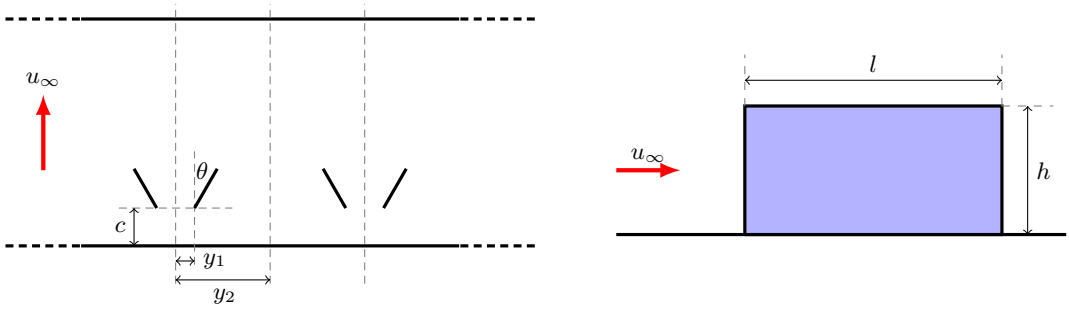

(a) Top view (b) Side view

Fig. 9: VG Configuration

Rectangular VGs are modelled in this work and the VGs are counter-rotating in nature. The five design parameters were chosen as these give a sufficient variation in the flow nature and final force coefficients to design for a chosen objective function. The maximum and minimum values of the design parameters are shown in table 2, and chosen to represent sensible coverage without including extremes of the design space; the range of h was chosen to represent variation in the boundary layer

thickness over the airfoil; AR range was chosen to represent typical VG design sizes; the angle range is considered to be a range where a flat plate provides effective lift; chord placement was chosen to be far enough upstream such that the vortex has time to develop and encourage mixing of the boundary layer with higher energy flow to become effective enough to avoid separation; s was chosen to be within limits to avoid very large meshes. All parameters were scaled such that the design space is $[0, 1]^5$.

Table 2: Design space range

Parameter	Minimum	Maximum
h	0.2%	2%
AR	1	4
θ	5°	30°
c	5%	60%
s	5	20

C. Surrogate Modelling

A surrogate model is an interpolation or approximation made from a small sample of data sites that give the value of the design space at those known data sites. A surrogate model can be formulated in a number of different ways, though the most common methods are by a polynomial [43], radial basis functions (RBFs) [44, 45] or Kriging [46–48]. Reviews of surrogate modelling and surrogate-based optimization have been presented [26–28], which the reader is guided to for more in-depth discussions on the formulations and common uses for each method. The surrogate model used in this work is developed around a multivariate interpolation using RBFs. This interpolation method has the advantage of providing exact recovery of data at the known sites, thus preserving the CFD data at the known sampled points.

The general theory of RBFs is presented by Buhmann[49] and Wendland [50], and the basis of the method used here is described in detail by Rendall and Allen [34] and surrogate specific detail in Mackman *et al.*[51]. Let $f(\mathbf{x})$ be the original function to be modelled, and f_i be the scalar

values at n discrete points $\mathbf{x}_i, i = 1, ..., n$, where $\mathbf{x}_i$ is the vector of inputs at the ith sample point in d-dimensional space $x^k, k = 1, ..., d$. The set of data points $\mathcal{X} = \{\mathbf{x}_1, ..., \mathbf{x}_n\}$ is confined to a domain Ω in d-dimensional space. A RBF model is then a linear combination of basis functions, whose argument is the Euclidean distance between the point $\mathbf{x}$ at which the interpolation is made and the n points in the known data set. If ϕ is the chosen basis function and $\|\cdot\|$ is used to denote the Euclidean norm, then an interpolation model q has the form:

$$q(\mathbf{x}) = \sum_{i=1}^{n} w_i \phi(\|\mathbf{x} - \mathbf{x}_i\|) + P(\mathbf{x}) \tag{2}$$

where $w_i, i = 1, ..., n$ are model coefficients, and $P(\mathbf{x})$ is an optional polynomial. The coefficients are found by requiring exact recovery of the original data, $\mathbf{q}_{\mathcal{X}} = \mathbf{f}$, for all points in the training data set $\mathcal{X}$. Hence the model is an interpolant, and all original solution information is preserved. When the polynomial term is included, the system is completed by the additional requirement

$$\sum_{i=1}^{n} w_i P(\mathbf{x}) = 0 \tag{3}$$

which is sometimes referred to as the side condition, for a polynomial that takes the form

$$P = \gamma_0 + \sum_{k=1}^{d} \gamma_k x^k \tag{4}$$

Setting up a global RBF interpolation then requires a solution to a linear system:

$$\begin{pmatrix} 0 \\ 0 \\ \vdots \\ 0 \\ f_1 \\ \vdots \\ f_n \end{pmatrix} = \begin{pmatrix} 0 & 0 & \cdots & 0 & 1 & \cdots & 1 \\ 0 & 0 & \cdots & 0 & x_1^1 & \cdots & x_n^1 \\ \vdots & \vdots & \ddots & \vdots & \vdots & \ddots & \vdots \\ 0 & 0 & \cdots & 0 & x_1^d & \cdots & x_n^d \\ 1 & x_1^1 & \cdots & x_1^d & \phi_{1,1} & \cdots & \phi_{1,n} \\ \vdots & \vdots & \ddots & \vdots & \vdots & \ddots & \vdots \\ 1 & x_n^1 & \cdots & x_n^d & \phi_{n,1} & \cdots & \phi_{n,n} \end{pmatrix} \begin{pmatrix} \gamma_0 \\ \gamma_1 \\ \vdots \\ \gamma_d \\ w_1 \\ \vdots \\ w_n \end{pmatrix} \tag{5}$$

where $\phi_{i,j} = \phi(\|\mathbf{x}_i - \mathbf{x}_j\|)$. Once the coefficients are known, the objective function at an interpolated point is then found by equation 2.

Many choices are available for the basis function itself, but a radial conditionally positive definite function is chosen to ensure the system has a unique solution. Basis functions are said to be compactly supported when they decay to zero at a given distance from the centre, known as the support radius R. Compactly supported functions have desirable numerical characteristics and modelling behaviour, hence the work presented here uses Wendland's C^2 function [50].

The support radius used in the function also acts to control the region of influence of each of the centres. A larger support radius allows each sample point to influence the interpolation at a given point from a greater distance away, and in general leads to a smoother interpolation. The support radius scales the Euclidean distance between two points:

$$\|\mathbf{x} - \mathbf{x}_i\|_{scaled} = \frac{1}{R}\sqrt{\sum_{k=1}^{d}(x^k - x_i^k)^2}. \tag{6}$$

D. Latin Hypercube Sampling

The surrogate-based approach relies on limiting the number of high fidelity sample points within the design space, and thus efficient design space interrogation methods are desired. A Latin Hypercube sampling approach [52] is a statistics-based approach designed to produce an optimum configuration of sample points through the design space; the design space produced has each division in all dimensions sampled by exactly one sample point. This approach is particularly useful in initial sampling as it incorporates many of the desirable properties of random sampling and stratified sampling [53].

In this work, LHC sampling was used to construct the initial design space. In addition, corners of the sample space were also added as this is important for the surrogate interpolation. Whilst a random LHC can be utilised, an optimised LHC offers an improvement in providing a more evenly sampled design space for construction of the surrogate model. The approach chosen utilised the Morris and Mitchell [54] Φ_p criteria. Since the possible combinations for a 5 dimension hypercube with only 100 sample points is of the order of 10^{790}, an optimization algorithm is required. This

work used the Enhanced Stochastic Evolution algorithm proposed by Jin *et al.* [55]. An example of the resulting Latin Hypercube sample is shown in figure 10 for 100 sample points in two-dimensions plus the corner points.

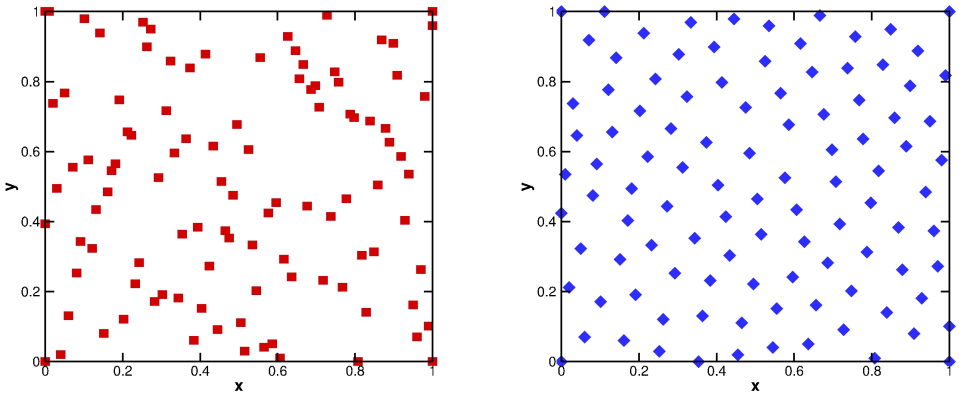

(a) Random LHC

(b) Optimized LHC

Fig. 10: Latin Hypercube sampled design space (plus corner points)

The Latin Hypercube used in this work consisted of 181 sample and corner points.

E. Adaptive Sampling

The Latin Hypercube sampling approach was used as a means of efficiently constructing the initial set of samples required to generate the first version of the surrogate model. Adaptive sampling then interrogates the surrogate model to determine new sampling locations. Once these locations were simulated, they were added in to the next version of the surrogate model. Using an adaptive approach allows better capture of the design space by the surrogate in the regions of interest [51]. Furthermore, the use of an adaptive sampling strategy compared to the equivalent cost of the conventional sampling, by say a Latin Hypercube, has been shown to lead to a much more accurate surrogate model with better capture of the variations and curvature of the design space [51].

Updated sampling points are generated based on a compromise between space-filling updates and local refinement in non-linear regions. This non-linearity is determined by the Laplacian. A smooth separation function quantifies the sample spacing in order to assess space-filling updates. A

criterion, C, was proposed in [29] which merges these two criteria:

$$C = (|\nabla^2 J| + \epsilon)(1 - H)^2 \qquad 0 \leq H \leq 1 \tag{7}$$

where ϵ is a small number, sufficient to avoid $C = 0$ when $|\nabla^2 J| = 0$. The variable H is the space-filling function, such that $(1 - H)$ grows away from previously sampled locations. However, this criterion C was proposed in order to improve information around both maxima and minima within the surrogate model (hence the magnitude of the Laplacian). If only a minimum is desired (positive Laplacian) or maximum (negative Laplacian) then the C function can be adjusted appropriately. Larger values of C indicate new potential sample locations.

The space-filling (or separation) function, H, is defined as a smooth function, for blending with the local refinement component of C. In this function, $H = 1$ at a sample point, and diminishes as distance increases away from the sample point. This is produced using an RBF kernel with a compactly supported basis function and small support radius. The support radius used in this work was determined as a function of two distances, the minimum distance (d_1) and supremum minimum distance (d_2) between sample points.

$$R_h = R_0 \sqrt{(d_1 d_2)} \tag{8}$$

where R_0 is a scaling factor, which typically has a value of approximately unity. However, it was found that the adaptive sampling approach outlined above was insufficient to progressively refine the solution without significant adaptive sample points. Therefore the adaptive sampling approach was modified with the addition of an exploitative term

$$C_b = (|\nabla^2 J| + \epsilon)(1 - H)^2 b^3 \tag{9}$$

where b is a distance based function used to force the adaptive sampling to place points around the current optimum. The b function is smooth and produced via an RBF kernel in the same manner as H. $b = 1$ at the optimum point and will decay away from the point to zero at the furthest reaches of

the design space. Thus the original adaptive sampling approach can be seen as primarily explorative (when $b = 1$ throughout the design space), whilst the new is exploitative ($0 \leq b \leq 1$). Furthermore, the new adaptive sampling approach balances three important requirements for an effective design space model; space-filling (due to the H function), curvature modelling (due to the Laplacian) and optimum locating (due to the b function). The performance of the new method was tested on two analytical design spaces, and the results are presented below.

1. Franke's Function

Franke's function is a bivariate function, consisting of two Gaussian peaks of differing heights and a smaller trough. In this instance, the adaptive sampling is undertaken using a grid evaluation seeking only the maximum location, with the trough refinement ignored. The function is defined using

$$\begin{aligned} f(\mathbf{x}) = 0.75\exp\left(-\frac{(9x_1-2)^2}{4} - \frac{(9x_2-2)^2}{4}\right) + 0.75\exp\left(-\frac{(9x_1+1)^2}{49} - \frac{9x_2+1}{10}\right) \\ +0.5\exp\left(-\frac{(9x_1-7)^2}{4} - \frac{(9x_2-3)^2}{4}\right) - 0.2\exp\left(-(9x_1-4)^2 - (9x_2-7)^2\right) \end{aligned} \tag{10}$$

between $x_i \in [0, 1]$.

After an initial 9 sample points, 24 adaptive sample points are introduced sequentially. The results for using both adaptive sampling techniques is given in figure 11.

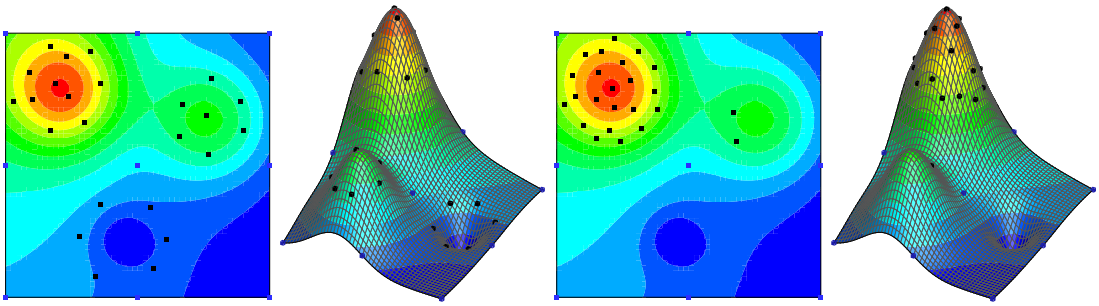

(a) C approach top view (b) C approach (c) C_b approach top view (d) C_b approach

Fig. 11: Comparison of C and C_b adaptive sampling approaches using Franke's Function

It is clear that the C_b approach produces samples that are highly concentrated around the

primary peak. it is also more rapid in identifying the exact peak location during the adaptive cycle.

2. Rastrigin Function

The two-dimensional variant of the n-dimensional Rastrigin function is a more complex problem, with a plethora of local minima and maxima. It is defined by

$$f(\mathbf{x}) = -An - \Sigma_{i=1}^{n} \left(x_i^2 - A\cos\left(2\pi x_i\right)\right) \tag{11}$$

where $A = 10$, $n = 2$, $x_i \in [-5.12, 5.12]$. The global maximum ($f(\mathbf{x}) = 0$) is located at $\mathbf{x} = 0$. After an initial 16 sample points, 24 adaptive sample points are introduced sequentially. As shown in figure 12, both adaptive approaches capture the overall global maximum, although the C_b function has again clearly covered all potential local maxima within proximity. Both adaptive strategies offer advantages, with C providing an initial adaptive coverage, and C_b refining the final solution.

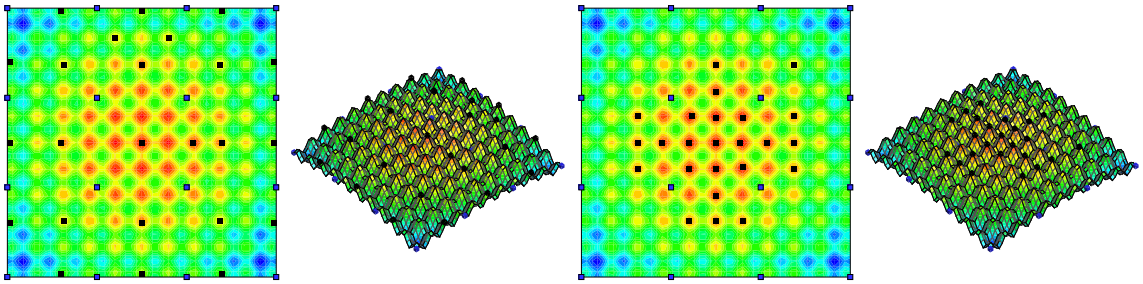

(a) C approach top view (b) C approach (c) C_b approach top view (d) C_b approach

Fig. 12: Comparison of C and C_b adaptive sampling approaches using Rastrigin's Function

F. Differential Evolution

The use of a global optimization algorithm coupled with a surrogate model provides for rapid determination of points of interest (for adaptive sampling) or the optimum solution itself. A global optimization approach was developed based on differential evolution (DE) [56]. DE is a swarm intelligence algorithm built around the concept of evolutionary mechanics. Like the other swarm intelligence algorithms DE takes a number of agents (parameter vectors) and follows three steps to advance the optimization algorithm:

1. *Mutation*: generate a mutated candidate solution by small, random changes

2. *Crossover*: 'breeding' of mutated and parent solutions to produce a child

3. *Selection*: accept the new child based on its fitness

The parameter vectors are vectors of length d, where each entry represents a position in each of the d design parameters:

$$\mathbf{x}_n = \{x_n^1, x_n^2, \ldots, x_n^d\}^T \tag{12}$$

The mutation stage involves the production of a new, candidate solution to introduce variability and exploration into the algorithm. The candidate/mutated solution for the n-th parent/target solution is called the donor vector, $\mathbf{v}_n$, and is produced by combining three existing parameter vectors:

$$\mathbf{v}_n = \mathbf{x}_{r_1^n} + F(\mathbf{x}_{r_2^n} - \mathbf{x}_{r_3^n}) \tag{13}$$

where r_1, r_2 and r_3 ($r_1 \neq r_2 \neq r_3 \neq n$) are random integers chosen from the range $[1, N]$, for a population of N parameter vectors (or agents), for each parent vector, and F is a scalar that is typically in the interval $[0, 1]$ and is chosen to either maximize or minimize exploration away from the existing agents. The crossover stage is used to enhance diversity in the population by combining aspects of the given parent and donor vectors. Binomial crossover, with probability CR is used in this work. Thus the DE variant employed was DE/rand/1/bin. The final stage of the algorithm is to assess whether the new child is of sufficient fitness to replace the given parameter vector. If the fitness of the child vector is better than its parent then the child replaces the parent.

The DE algorithm was run with constants commonly found in the literature [57]; 50 particles, crossover probability 0.3, mutation rate 0.7. A four stage population stage reduction (PSR) [58] was also used to aid convergence.

IV. Results

In this section, the results obtained from the adaptive surrogate optimization process for the design of VGs are presented. The airfoil used is the NACA 64(4)-421 section with a 0.4% chord blunt trailing edge. Results are presented summarising the initial sampling points obtained using LHC sampling and run using the CFD framework. A summary of the surrogate model is then presented. Finally, optimization results and adaptive sampling results are presented showing the optimized VG geometry.

A. Latin Hypercube Sampling Summary

At all Latin Hypercube samples the airfoil was trimmed to the design loading of $C_L = 1.3$. A brief statistical summary of the results is shown in table 3.

Table 3: Design space results

	Parameter	Value	h	AR	θ	c	s
	C_D	0.0203					
Min. J	Separation	0.1%	0.82%	3.84	16.89°	55.6%	8.8
	J	0.0204					
	C_D	0.0784					
Max. J	Separation	0.0%	1.98%	2.98	27.00°	15.73.0%	10.17
	J	0.0784					
	C_D	0.0178					
Min. C_D	Separation	10.4%	1.72%	2.58	22.75°	37.45%	18.05
	J	0.0230					
	C_D	0.0784					
Max. C_D	Separation	0.0%	1.98%	2.98	27.00°	15.73%	10.17
	J	0.0784					
	C_D	0.0263					
Max. S	Separation	17.4%	1.89%	1.87	13.13°	59.45%	13.16
	J	0.0349					

It is evident from table 3 that considering drag in isolation is not sufficient to reduce (and

eliminate) separation. Of the 181 samples, 24.5% have $S < 0.1\%$, but only two (4.4%) of this reduced sample have a $C_D < 0.0210$. These two samples are spread throughout the design space, such that the distance between these points with the normalised $[0, 1]^5$ design space is 0.85 which equates to 38% of the design space range.

B. Surrogate Model

The initial surrogate model was constructed using Wendland's C2 function with a support radius sufficient to cover the entire design space. Selected projections for the objective function J are presented in figure 13 for the design space $[0, 1]^5$.

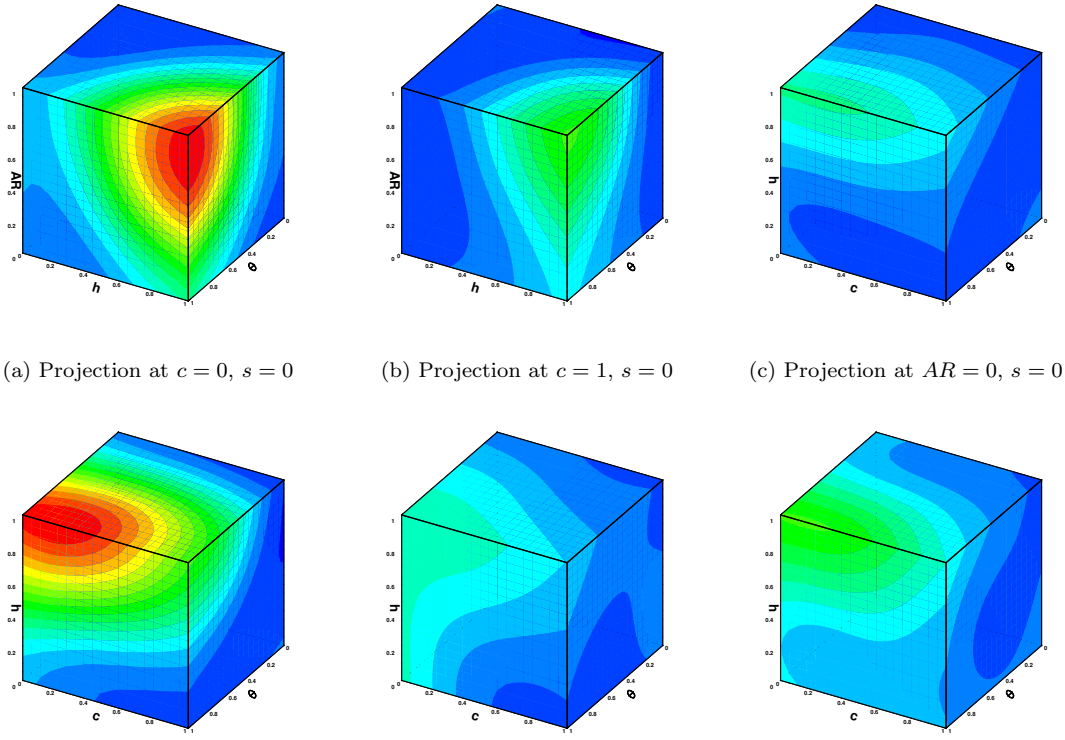

(a) Projection at $c = 0$, $s = 0$ (b) Projection at $c = 1$, $s = 0$ (c) Projection at $AR = 0$, $s = 0$

(d) Projection at $AR = 1$, $s = 0$ (e) Projection at $AR = 0$, $s = 1$ (f) Projection at $AR = 1$, $s = 1$

Fig. 13: Surrogate model projections (blue represents lower objective, J)

C. Optimization

The results of optimizing the VG surrogate model for the objective function given by equation 1 are given in table 4, along with the clean values and the values that are the lowest objective values

from the latin hypercube sample. To increase the adaptive sampling rate, a number of updates per iteration were undertaken in parallel. This only requires updating the separation function before determination of the next update location. The number of updates per iteration and the number of iterations was prescribed in advance. Two iterations of adaptive sampling using five samples in each iterations were performed.

Table 4: Design space results

	J	C_D	Separation	α	h	AR	θ	c	s
Clean	0.0247	0.0191*	11.1%*	9.6°	-	-	-	-	-
Min. LHC	0.0204	0.0203	0.1%	9.0°	0.81%	3.84	16.89°	55.6%	8.8
Optimized (Surrogate)	0.0189	–	–	8.8°	0.85%	3.64	8.42°	21.5%	5.8
Optimized (CFD)	0.0189	0.0189	0.0%						

* oscillatory result: time-averaged

The results clearly demonstrate that the optimized value is a considerable improvement in the separation experienced on the airfoil and therefore a reduction in buffet may be expected. The optimization process via differential evolution has also improved the performance of the VG compared to just taking the best sample tested in the latin hypercube, therefore vindicating the optimization process. Comparing to the clean geometry, it is particularly impressive that the process developed here, of design space sampling, surrogate-based optimization and adaptive sampling, has been able to eliminate separation at a highly loaded condition and achieved a decrease in the drag on the airfoil of 7% relative to best result achieved by the Latin hypercube sampling alone.

Figure 14 shows the (span-averaged) pressure coefficients and the (span-averaged) upper surface streamwise skin friction coefficients (figure 15 shows the skin friction near to the trailing edge) of the clean geometry and with the optimized VG. Streamlines proximal to the VG and trailing edge of the airfoil are presented in figure 16. The large separation region rearwards of $x/c = 89\%$ present in the clean geometry has been entirely eliminated using the optimum VG configuration; see figure 8 for the clean geometry streamlines. This is also clearly shown in the skin friction coefficients. Figure 17 shows the vortex extent, as defined by the $\lambda_2 = 0$ criterion between the minimum LHC sample

and the optimum solution. The induced vortex of the optimum design has eliminated separation at the trailing edge of the airfoil, as shown in figure 16, although a small region is still present in the minimum LHC sample.

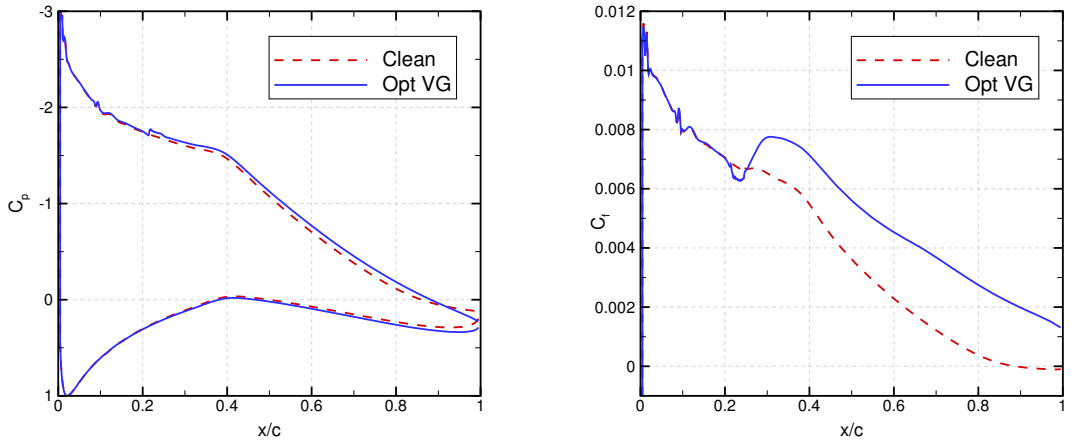

(a) Pressure

(b) Skin friction

Fig. 14: Span-averaged pressure and upper surface streamwise skin friction coefficients

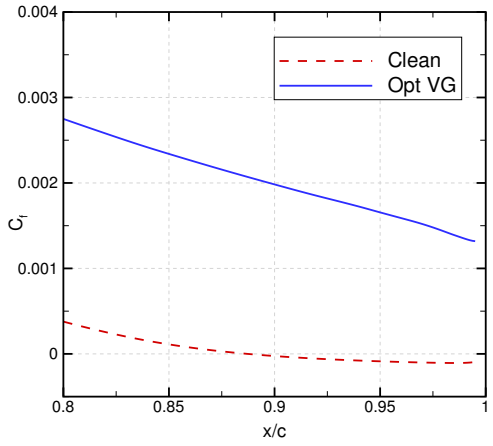

Fig. 15: Trailing edge span-averaged upper surface streamwise skin friction coefficients

Angle of attack sweeps were also performed on the clean airfoil (initial design) and the airfoil with optimized VG (optimum design) to analyse the off-design performance at the design flow conditions, and these are presented in figure 18 (the clean wing was run until stall onset). It can be seen that the angle at which separation has occurred has been increased considerably using the optimum VG, indicating that the optimization has produced an improvement along a wide range of

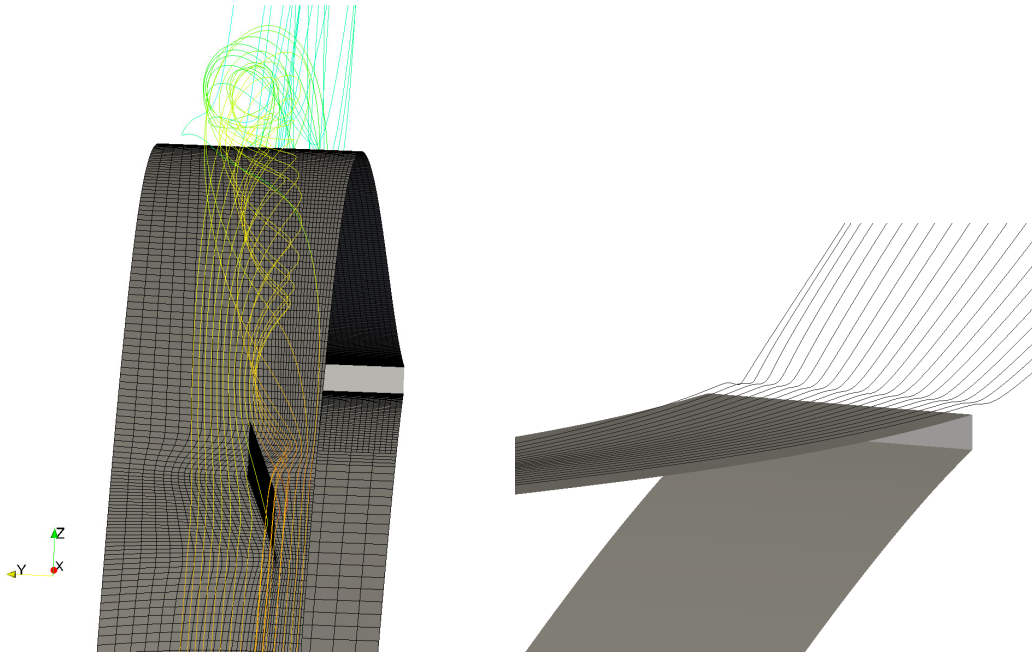

Fig. 16: Induced vortex impact downstream of optimized VG

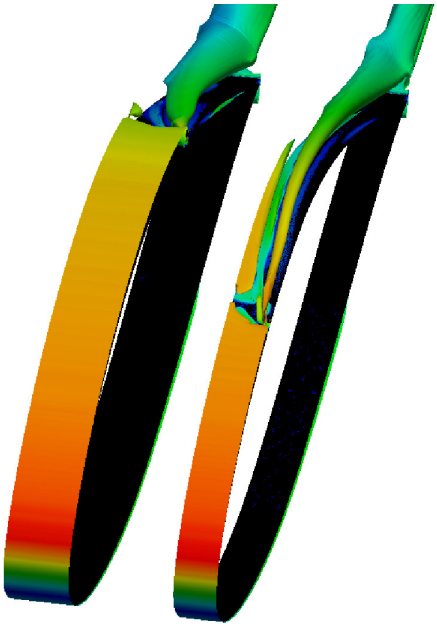

Fig. 17: Vortex extent from minimum LHC (left) and fully optimized VG (right)

the angle of attack, and not just at the design point.

As previously stated, VGs are added to cure flow issues at design points that are generally away from cruise, often an the extremes of the flight envelope, and this has been considered here. As such, the VGs will give a performance penalty in cruise where they are not actively providing a positive

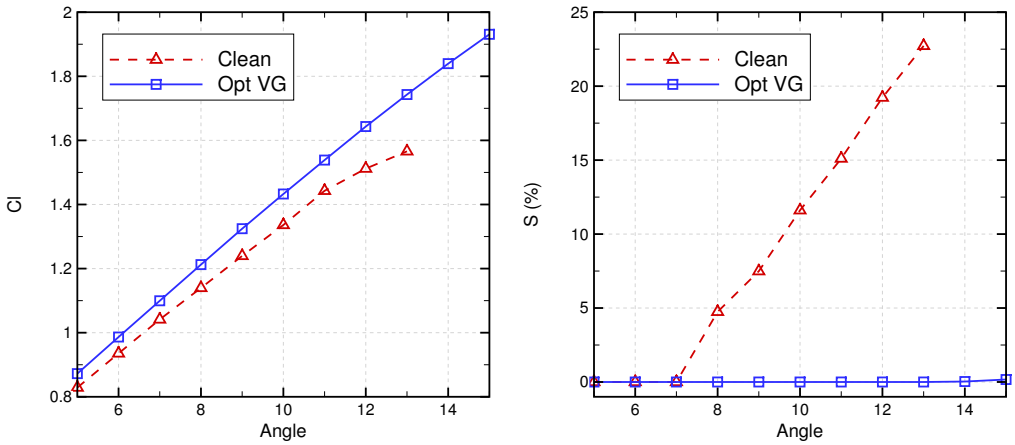

(a) Lift

(b) Separation

Fig. 18: Angle of attack sweeps of clean airfoil and optimized VG at design condition

influence. Hence, sweeps have been performed at a representative cruise condition ($M = 0.45$, $Re = 8.7$ million) and the lift-drag polar is given in figure 19. **A tiltrotor aircraft maintains the vertical take-off and landing capability of a conventional helicopter but with a much higher cruise speed, range and endurance, close to that of a conventional fixed wing aircraft. To achieve this, in the cruise conditions, the wing design objectives are generally low drag and a high L/D ratio. As noted, however, the VGs – which are required for buffet mitigation – provide a drag penalty in cruise and at a typical cruise C_L, the L/D penalty by adding the VGs is 12%. Therefore, for the cruise condition of this infinite wing, perhaps a large penalty to the performance of the wing in the primary flight condition is not desirable, though, as also noted, if buffet is an issue in an off-design flight condition then VGs may be necessary along with the associated cruise performance penalty. In tiltrotor design, as in all engineering design, trade-offs, which here are between cruise performance and the buffet mitigation, are critical.**

Finally, to demonstrate that the optimization process has converged onto a minimum value, the value of the gradients of the objective with respect to changes in the design variables at the optimized point were considered. An optimum solution for this type of problem is one where the gradient values approach a very small number. Table 5 shows these gradient values and demonstrates

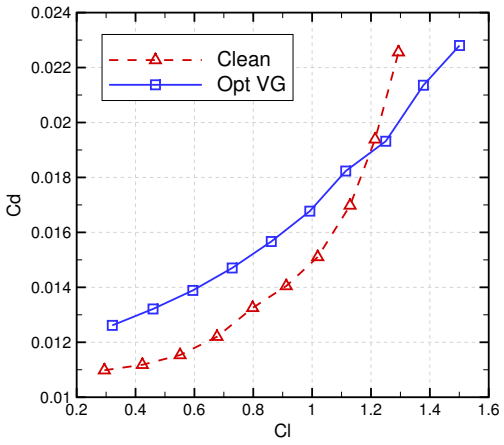

Fig. 19: Lift-drag polars of clean airfoil and optimized VG at cruise flow conditions

the high performance of the optimization algorithm. This is further demonstrated in figure 20, where the convergence of the optimizer is terms of the chord location design variable shows convergence onto a single solution. Furthermore, the use of the adaptive sampling strategy to improve the prediction of the surrogate model is vindicated; figure 20 demonstrates that by performing adaptive sampling, the error between the predicted optimal objective function from the surrogate, and the actual objective function from the CFD, converges, such that the error after two rounds of adaptive sampling is 0.42%, or less than 1 drag count.

Table 5: Gradients at minimum LHC sample and optimum solution

	Min. LHC	Optimized
$\partial J/\partial h$	6.2×10^{-3}	-2.3×10^{-10}
$\partial J/\partial AR$	-1.3×10^{-2}	1.2×10^{-9}
$\partial J/\partial \theta$	3.0×10^{-3}	-3.8×10^{-11}
$\partial J/\partial c$	3.2×10^{-3}	7.1×10^{-10}
$\partial J/\partial s$	-4.2×10^{-3}	1.5×10^{-9}

V. Conclusion

The quantification of the effects of flow around a tiltrotor-like airfoil with vortex generators (VGs) and subsequent design of these VGs has been considered. The highly loaded and thick wing

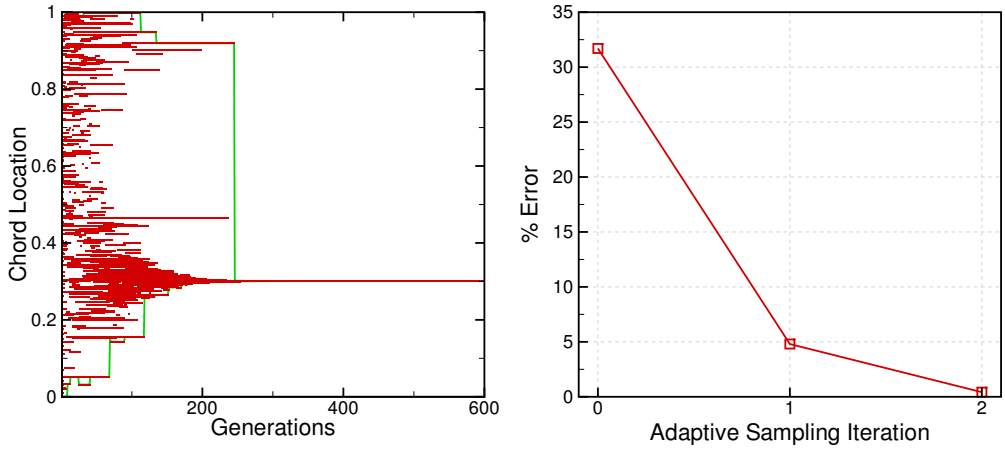

(a) Differential Evolution

(b) Adaptive sampling

Fig. 20: Convergence rate of optimizer to optimal design for chord location, and convergence of surrogate error after adaptive sampling.

of a tiltrotor is particularly susceptible to early onset buffet, so boundary layer control is critical and, hence, upper surface flow control devices are an important consideration. An analysis package has been developed that uses the open source library, OpenFOAM, to obtain high-fidelity viscous flow simulation, and a custom mesh generator to autonomously obtain high quality structured meshes for VGs on a wing.

Design of counter rotating VGs has been considered using, first, a Latin Hypercube sampling approach to obtain design space samples for five variables; VG height, VG aspect ratio, VG angle, chord-wise location, and VG spacing. A surrogate model that uses radial basis functions has been developed to produce an approximation to a high-fidelity design space but still preserves the important flow physics required for design. An optimization algorithm based on differential evolution, which is a global search algorithm, was used to fully interrogate the surrogate model design space. With the initial sample points defined via an optimised Latin Hypercube, adaptive sampling using a new, integrated criterion was developed that balances the requirements of space-filling, curvature modelling and optimum locating. This optimization strategy, of adaptive surrogate modelling was used to optimize VG design for a high-loading tiltrotor condition, representative of a flight condition on the edge of the flight envelope where the wing is highly loaded. The objective function blends

the requirement for drag minimization with reduction of separation.

The objective of the design is to reduce drag of the airfoil while also eliminating separation, which is a major cause of early-onset buffet in tiltrotors. Results demonstrate that using this framework allows elimination of the separation using VGs. A particularly impressive result obtained is that the drag of the wing with optimized VG is lower than the drag of the clean wing. Furthermore, the off-design performance of the optimized VG shows the elimination of separation up to large angles of attack, and therefore a considerable reduction in drag at those large angles, **however a design trade-off needs to be considered between buffet elimination at the design point considered and the cruise performance, which is otherwise reduced.**

Acknowledgments

The authors would like to thank David Tring and Nigel Scrase of AgustaWestland, for their support of and contribution to this work. The financial support, via the HiPerTilt project, of AgustaWestland and Innovate UK (Technology Strategy Board) is also gratefully acknowledged. Finally, the authors would like to acknowledge that this work was carried out using the computational facilities of the Advanced Computing Research Centre, University of Bristol.

References

[1] Maisel, M., Giulianetti, D., and Dugan, D., "The History of the XV-15 Tilt Rotor Research Aircraft: From Concept to Flight," Tech. Rep. SP 2000-4517, NASA, 2000.

[2] Lin, J. C., "Review of research on low-profile vortex generators to control boundary-layer separation," *Progress in Aerospace Sciences*, Vol. 38, No. 4–5, 2002, pp. 389–420.
doi:10.1016/S0376-0421(02)00010-6.

[3] Weiberg, M., J.A. Maisel, "Wind-tunnel tests of the XV-15 tilt rotor aircraft," Tech. Rep. TM 81177, NASA, 1980.

[4] Abras, J. and Narducci, R., "Analysis of CFD Modeling Techniques over the MV-22 Tiltrotor," *66th American Helicopter Society International Annual Forum*, Phoenix,Arizona, 2010.

[5] Tai, T., "Effect of Midwing Vortex Generators on V-22 Aircraft Forward-Flight Aerodynamics," *Journal of Aircraft*, Vol. 40, No. 4, 2003, pp. 623–630.
doi:10.2514/2.3165.

[6] Hamstra, J. W., Miller, D. N., and Truax, P. P., "Active Inlet Flow Control Technology Demonstration," *22nd International Congress of Aeronautical Sciences*, 2000, pp. Harrogate, UK, ICAS-2000-6.11.2.

[7] Li, Q. and Liu, C., "Declining Angle Effects of the Trailing Edge of a Microramp Vortex Generator," *Journal of Aircraft*, Vol. 47, No. 6, 2010, pp. 2086–2095.
doi:10.2514/1.C000318.

[8] Ito, Y., Murayama, M., and Yamamoto, K., "High-Quality Unstructured Hybrid Mesh Generation for Capturing Effects of Vortex Generators," *51st AIAA Aerospace Sciences Meeting including the New Horizons Forum and Aerospace Exposition*, Grapevine, Texas, 2013, AIAA Paper 2013–554.
doi:10.2514/6.2013-554.

[9] Konig, B., Fares, E., and Nolting, S., "Fully-Resolved Lattice-Boltzmann Simulation of Vane-Type Vortex Generators," *7th AIAA Flow Control Conference*, Alanta, Georgia, 2014, AIAA Paper 2014–2795.
doi:10.2514/6.2014-2795.

[10] Allan, B. G., Yao, C.-S., and Lin, J. C., "Numerical Simulations of Vortex Generator Vanes and Jets on a Flat Plate," *1st AIAA Flow Control Conference*, St Louis, Missouri, 2002, AIAA Paper 2002–3160.
doi:10.2514/6.2002-3160.

[11] Wik, E. and Shaw, S. T., "Numerical Simulation of Micro Vortex Generators," *2nd AIAA Flow Control Conference*, Portland, Oregon, 2004, AIAA Paper 2004–2697.
doi:10.2514/6.2004-2697.

[12] Dandois, J., Brunet, V., Molton, P., Abart, J.-C., and Lepage, A., "Buffet Control by Means of Mechanical and Fluidic Vortex Generators," *5th AIAA Flow Control Conference*, Chicago, Illinois, 2010, AIAA Paper 2010–4975.
doi:10.2514/6.2010-4975.

[13] Lu, F. K., Pierce, A. J., Shih, Y., Lin, C., and Li, Q., "Experimental and Numerical Study of Flow Topology Past Micro Vortex Generators," *40th AIAA Fluid Dynamics Conference and Exhibit*, Chicago, Illinois, 2010, AIAA Paper 2010–4463.
doi:10.2514/6.2010-4463.

[14] Memory, C., Snyder, D. O., and Bons, J., "Numerical Simulation of Vortex Generating Jets in Zero and Adverse Pressure Gradients," *46th AIAA Aerospace Sciences Meeting and Exhibit*, Reno, Nevada, 2008, AIAA Paper 2008–558.
doi:10.2514/6.2008-558.

[15] Forster, K. J. and White, T. R., "Numerical Investigation into Vortex Generators on Heavily Cambered

Wings," *AIAA Journal*, Vol. 52, No. 5, 2014, pp. 1059–1071.
doi:10.2514/1.J052529.

[16] Kunik, W. G., "Application of a Computational Model for Vortex Generators in Subsonic Internal Flows," *AIAA/ASME/SAE/ASEE 22nd Joint Propulsion Conference*, Huntsville, Alabama, 1986, AIAA Paper 1986–1458.
doi:10.2514/6.1986-1458.

[17] Bender, E. E., Anderson, B. H., and Yagle, P. J., "Vortex Generator Modeling for Navier-Stokes Codes," *American Society of Mechanical Engineers*, 1999, FEDSM 99-6929.

[18] Jirasek, A., "Vortex-Generator Model and Its Application to Flow Control," *Journal of Aircraft*, Vol. 42, No. 6, 2005, pp. 1486–1491.
doi:10.2514/1.12220.

[19] Dudek, J. C., "Modeling Vortex Generators in a Navier-Stokes Code," *AIAA Journal*, Vol. 49, No. 4, 2011, pp. 748–759.
doi:10.2514/1.J050683.

[20] Spalart, P. R. and Allmaras, S. R., "A One-Equation Turbulence Model for Aerodynamic Flows," *Recherche Aerospatiale*, Vol. 1, 1994, pp. 5–21.

[21] Menter, F. R., "Two-equation Eddy-viscosity Turbulence Model for Engineering Applications," *AIAA Journal*, Vol. 32, No. 8, 1994, pp. 1598–1605.
doi:10.2514/3.12149.

[22] Yaras, M. I. and Grosvenor, A. D., "Evaluation of one- and two-equation low-Re turbulence models. Part II–Vortex-generator jet and diffusing S-duct flows," *International Journal for Numerical Methods in Fluids*, Vol. 42, No. 12, 2003, pp. 1321–1343.
doi:10.1002/fld.587.

[23] Lee, S., Loth, E., and Babinsky, H., "Normal shock boundary layer control with various vortex generator geometries," *Computers and Fluids*, Vol. 49, No. 1, 2011, pp. 233–246.
doi:10.1016/j.compfluid.2011.06.003.

[24] Shan, H., Jiang, L., Liu, C., Love, M., and Maines, B., "Numerical Study of Passive and Active Flow Separation Control over a NACA0012 Airfoil," *Computers and Fluids*, Vol. 37, No. 8, 2008, pp. 975–992.
doi:10.1016/j.compfluid.2007.10.010.

[25] Yi, J., Kim, C., and Lee, B. J., "Adjoint-Based Design Optimization of Vortex Generator in an S-Shaped Subsonic Inlet," *AIAA Journal*, Vol. 50, No. 11, 2012, pp. 2492–2507.
doi:10.2514/1.J051687.

[26] Jones, D. R., "A Taxonomy of Global Optimization Methods Based on Response Surfaces," *Journal of Global Optimization*, Vol. 21, No. 4, 2001, pp. 345–383.
doi:10.1023/A:1012771025575.

[27] Queipo, N. V., Haftka, R. T., Shyy, W., Goel, T., Vaidyanathan, R., and Tucker, P. K., "Surrogate-based analysis and optimization," *Progress in Aerospace Sciences*, Vol. 41, 2005, pp. 1–28.
doi:10.1016/j.paerosci.2005.02.001.

[28] Forrester, A. I. J. and Keane, A. J., "Recent advances in surrogate-based optimization," *Progress in Aerospace Sciences*, Vol. 45, 2009, pp. 50–79.
doi:10.1016/j.paerosci.2008.11.001.

[29] Mackman, T. J. and Allen, C. B., "Investigation of an adaptive sampling method for data interpolation using radial basis functions," *International Journal for Numerical Methods in Engineering*, Vol. 83, 2010, pp. 915–938.
doi:10.1002/nme.2885.

[30] Jirasek, A., "Design of Vortex Generator Flow Control in Inlets," *Journal of Aircraft*, Vol. 43, No. 6, 2006, pp. 1886–1892.
doi:10.2514/1.21364.

[31] Kuya, Y., Takeda, K., Zhang, X., and Forrester, A. I. J., "Multifidelity Surrogate Modeling of Experimental and Computational Aerodynamic Data Sets," *AIAA Journal*, Vol. 49, No. 2, 2011, pp. 289–298.
doi:10.2514/1.J050384.

[32] Namura, N., Obayashi, S., and Jeong, S., "Efficient Global Optimization of Vortex Generators on a Super Critical Infinite-Wing Using Kriging-Based Surrogate Models," *52nd Aerospace Sciences Meeting and Exhibit*, National Harbor, Maryland, 2014, AIAA Paper 2014–904.
doi:10.2514/6.2014-0904.

[33] Allen, C. B., "Towards automatic structured multiblock mesh generation using improved transfinite interpolation," *International Journal for Numerical Methods in Engineering*, Vol. 74, No. 5, 2008, pp. 697–733.
doi:10.1002/nme.2170.

[34] Rendall, T. C. S. and Allen, C. B., "Unified Fluid–Structure Interpolation and Mesh Motion Using Radial Basis Functions," *International Journal for Numerical Methods in Engineering*, Vol. 74, No. 10, 2008, pp. 1519–1559.
doi:10.1002/nme.221.

[35] Rendall, T. C. S. and Allen, C. B., "Efficient Mesh Motion Using Radial Basis Functions with Data

Reduction Algorithms," *Journal of Computational Physics*, Vol. 228, No. 17, 2009, pp. 6231–6249. doi:10.1016/j.jcp.2009.05.013,.

[36] Yao, C.-S., Lin, J. C., and Allan, B. G., "Flow-Field Measurements of Device-Induced Embedded Streamwise Vortex on a Flat Plate," *1st AIAA Flow Control Conference*, St. Louis, Missouri, 2002, AIAA Paper 2002–3162.
doi:10.2514/6.2002-3162.

[37] Seal, D. M., "A Survey of Buffeting Loads," Tech. rep., Aeronautical Research Council, Ministry of Aviation, 1962, CP 584.

[38] Bore, C. L., "Post-Stall Aerodynamics of the 'Harrier' GR1," in "Fluid Dynamics of Aicraft Stalling," AGARD, 1972, AGARD Proceedings 102 and Report AD-753 441.

[39] Kenway, G. K. W. and Martins, J. R. R. A., "High-fidelity aerostructural optimization considering buffet onset," *16th AIAA/ISSMO Multidisciplinary Analysis and Optimization Conference*, Dallas, Texas, 2015, AIAA Paper 2015–2790.
doi:10.2514/6.2015-2790.

[40] Zastawny, M., "Numerical simulation of wing vortex generators – methodologies and validation," *The Aeronautical Journal*, Vol. 120, 2016, pp. 627–650.
doi:10.1017/aer.2016.13.

[41] Maisel, M., "NASA/Army XV-15 Tilt Rotor Research Aircraft Familiarization Document," Tech. Rep. TM X-62 407, NASA, 1975.

[42] Jeong, J. and Hussain, F., "On the identification of a vortex," *Journal of Fluid Mechanics*, Vol. 285, 1995, pp. 69–94.
doi:10.1017/S0022112095000462.

[43] Box, G. E. P. and Draper, N. R., *Empirical Model-Building and Response Surfaces*, Wiley, 1987.

[44] Broomhead, D. S. and Lowe, D., "Multivariable Function Interpolation and Adaptive Networks," *Complex Systems*, Vol. 2, No. 3, 1988, pp. 321–355.

[45] Sobester, A., Leary, S. J., and Keane, A. J., "On the Design of Optimization Strategies Based on Global Response Surface Approximation Models," *Journal of Global Optimization*, Vol. 33, No. 1, 2005, pp. 31–59.
doi:10.1007/s10898-004-6733-1.

[46] Krige, D. G., "A statistical approach to some basic mine valuation problems on the Witwatersrand," *Journal of the Chemical, Metallurgical and Mining Society of South Africa*, Vol. 53, No. 5, 1952, pp. 159–162.

[47] Sacks, J., Schiller, S. B., and Welch, W. J., "Designs for Computer Experiments," *Technometrics*, Vol. 31, No. 1, 1989, pp. 41–47.
doi:10.2307/1270363.

[48] Jones, D. R., Schonlau, M., and Welch, W. J., "Efficient Global Optimization of Expensive Black-Box Functions," *Journal of Global Optimization*, Vol. 13, No. 4, 1998, pp. 455–492.
doi:10.1023/A:1008306431147.

[49] Buhmann, M., *Radial Basis Functions*, Cambridge University Press, 1st ed., 2005.

[50] Wendland, H., *Scattered Data Approximation*, Cambridge University Press, 1st ed., 2005.

[51] Mackman, T. J., Allen, C. B., Ghoreyshi, M., and Badcock, K. J., "Comparison of Adaptive Sampling Methods for Generation of Surrogate Aerodynamic Models," *AIAA Journal*, Vol. 51, No. 4, 2013, pp. 797–808.
doi:10.2514/1.J051607.

[52] McKay, M. D., Beckman, R. J., and Conover, W. J., "A Comparison of Three Methods for Selecting Values of Input Variables in the Analysis of Output from a Computer Code," *Technometrics*, Vol. 21, No. 2, 1979, pp. 239–245.
doi:10.1080/00401706.2000.10485979.

[53] Helton, J. and Davis, F., "Latin hypercube sampling and the propagation of uncertainty in analyses of complex systems," *Reliability Engineering and System Safety*, Vol. 81, No. 1, 2003, pp. 23–69.
doi:10.1016/S0951-8320(03)00058-9.

[54] Morris, M. D. and Mitchell, T. J., "Exploratory designs for computational experiments," *Journal of Statistical Planning and Inference*, Vol. 43, 1995, pp. 381–402.
doi:10.1016/0378-3758(94)00035-T.

[55] Jin, R., Chen, W., and Sudjianto, A., "An efficient algorithm for constructing optimal design of computer experiments," *Journal of Statistical Planning and Inference*, Vol. 134, 2005, pp. 268–287.
doi:10.1016/j.jspi.2004.02.014.

[56] Storn, R. and Price, K., "Differential Evolution - A simple and efficient adaptive scheme for global optimization over continuous spaces," Tech. rep., ICSI, UC Berkeley, 1995, TR-95-012.

[57] Das, S. and Suganthan, P. N., "Differential Evolution: A Survey of the State-of-the-Art," *IEEE Transactions on Evolutionary Computation*, Vol. 15, No. 1, 2011, pp. 4–31.
doi:10.1109/TEVC.2010.2059031.

[58] Brest, J. and Maucec, M. S., "Population size reduction for the differential evolution algorithm," *Applied Intelligence*, Vol. 29, No. 3, 2008, pp. 228–247.

doi:10.1007/s10489-007-0091-x.